ACS APPLIED MATERIALS & INTERFACES

Research Article

www.acsami.org

Structure and Macroscopic Tackiness of Ultrathin Pressure Sensitive Adhesive Films

Alexander Diethert,[†] Volker Körstgens,[†] David Magerl,[†] Katharina Ecker,[†] Jan Perlich,[‡] Stephan V. Roth,[‡] and Peter Müller-Buschbaum*[,†]

[†]Technische Universität München, Physik-Department, Lehrstuhl für Funktionelle Materialien, James-Franck-Str.1, 85748 Garching, Germany

[‡]HASYLAB at DESY, Notkestr. 85, 22607 Hamburg, Germany

ABSTRACT: Ultrathin layers of the statistical copolymer P(nBA-stat-MA) with a majority of *n*-butyl acrylate (nBA) and a minority of methyl acrylate (MA) are characterized with respect to the film morphology and the mechanical response in a probe tack test. The probed copolymer can be regarded as a model system of a pressure sensitive adhesive (PSA). The films are prepared by spin-coating which enables an easy thickness control via the polymer concentration of the solution. The film thickness is determined with x-ray reflectivity (XRR) and white light interferometry (WLI). Grazing incidence small angle x-ray scattering (GISAXS) provides detailed and statistically significant information about the film morphology. Two types of lateral structures are identified and no strong correlation of these structures with the PSA film thickness is observed. In contrast, prominent parameters of the probe tack test, such as the stress maximum and the tack energy, exhibit an exponential dependence on the film thickness.

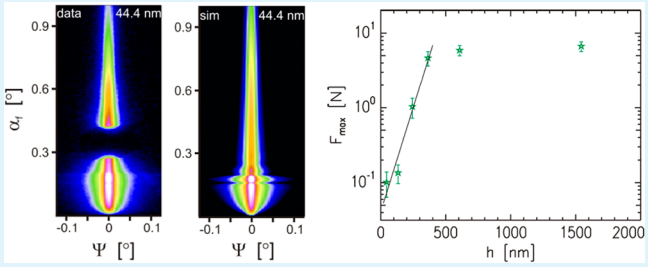

KEYWORDS: *pressure sensitive adhesive, GISAXS, thin film, tack, structure, statistical copolymer*

1. INTRODUCTION

The fabrication of very thin adhesive layers of only a few micrometers or even below is attracting more and more interest. A similar approach, for example, is to use self-assembled monolayers, which can influence the adhesion between two materials.[1−3] Our investigation, however, addresses the performance of the adhesive itself. We choose spin-coating as a well-established processing method to produce thin films over a wide thickness range of approximately three orders of magnitude. Possible areas of application of these ultrathin films are such, where the downsizing of devices is an important issue. Examples are microelectronic circuits,[4] micro-devices for the analysis of biological nanoparticles,[5] micro-patterned surfaces,[6] and polymer photonic devices.[7]

It is well-known that many properties of polymeric films deviate from bulk behavior when the film thickness goes a certain limit.[8] This holds for example for the morphology[9,10] or the thermal expansion coefficient.[11] But also material properties, which are more directly connected with tackiness, can be strongly affected. Among them is the glass transition temperature whose film thickness dependence is still under strong debate. Depending on the probed film-substrate combination and the applied experimental technique[12−15] different behavior was reported. In case the glass transition was observed to be dependent on the film thickness,[16,17] a limiting thickness of 150 nm is a reasonable estimate below which the glass transition temperature was seen to deviate from the bulk value.

Closely related to the value of the glass transition temperature are the mechanical properties of the material under investigation at a fixed temperature. In this context, Akabori et al. discovered with the use of lateral force microscopy an additional surface relaxation process for films that are thinner than a certain threshold value.[18] A direct access to viscoelastic parameters of ultrathin films, however, remains difficult due to technical reasons. Nevertheless, there are some direct measurements using for example a surface forces apparatus[19,20] or an atomic force microscope (AFM).[21] But also indirect techniques like buckling-based metrology,[22] thermal wrinkling,[23] and dewetting experiments[24] can be meaningful routes to investigate the viscoelastic behavior.

Pressure sensitive adhesives (PSAs) are usually very soft and highly dissipative. PSAs typically stick on a variety of different surfaces under low pressure in short time without any solvent evaporation or chemical reactions. In the early stage of the PSA debonding process cavities play a crucial role in the mechanical response (stress−strain curve).[25−28] These cavities can be generated in the bulk of the adhesives, as well as at the interface of the PSA.[25] As a consequence a change in the PSA film thickness will affect the cavity generation and thus the PSA performance.

Received: May 3, 2012
Accepted: July 20, 2012
Published: July 20, 2012

In case of block copolymer-based PSAs, a special morphology is installed by micro-phase separation.[29] In the micro-phase separation structure, the energy dissipation is increased substantially by a reduction in the fraction of bridging chains between glassy domains in the structure.[27] Thus film thickness induced changes of the bridging will cause an altered mechanical performance. Moreover, entanglements contribute to the modulus at low stresses.[27] As chain ends are enriched at surfaces and interfaces, the entanglement density at interfaces differs from that in the bulk. Given all these contributions, deviations in the mechanical behavior between bulk and thin film PSA samples are expected.

Adhesive properties of ultrathin films are often probed with so-called nano-tack or atomic force microscopic adhesion measurements.[30,31] With such methods, it was even possible to probe the adhesion and deformation of a single nanoscopic latex particle.[32] These phenomena, however, involve forces in the nN regime and only become visible at very short length scales. As a consequence, they are not suitable to describe the macroscopic tackiness. Although so far only established for much thicker films, an accurate measure for the adhesive performance can be obtained in a so-called probe tack test, in which a cylindrical punch with a diameter of several millimeters contacts an adhesive surface and force-distance curves are monitored during retraction. Therefore, in this study we use the probe tack test to focus on the macroscopic performance of ultrathin adhesive films.

The question we answer is what happens to the tackiness when the confinement in a probe tack test increases. Confinement in this study is not used in the sense of investigating films with thicknesses which are smaller than two times the radius of gyration of the polymer[15] as our ultrathin films are significantly thicker. In the present context of probe tack tests, the confinement is the ratio of the punch radius to the film thickness. In other words, when the punch radius is kept constant, the confinement increases with decreasing film thickness.

So far it has already been shown that the confinement is an important parameter in tack experiments.[33−35] Because of the experimental difficulties, there are not many studies which try to maximize the confinement. To our knowledge the highest confinement values reported in probe tack tests in literature[36] are below 10^2 and there are predictions concerning the failure modes up to 10^3. In the presented experimental work, however, we reach a confinement value of 2.3×10^4.

In addition to the investigation of the tackiness, we provide a full morphological characterization derived from grazing incidence small angle x-ray scattering (GISAXS) experiments.[37−41] For the first time, the existence of lateral structures exceeding simple surface roughness is proven and quantified for statistical copolymer based PSAs. However, it has to be noted that such three dimensional (3D) structuring is a well-investigated phenomenon for many other, non-adhesive systems consisting for example of block copolymers,[42−45] multiblock copolymers[46,47] or polymer blends.[48,49] In the case of PSA films, lateral structures have already been observed for example for styrene-diene block copolymers.[50] Also when poly(*n*-butyl acrylate) (PnBA) blended[51,52] or copolymerized[53] with polystyrene (PS) was chosen as a sample system, different morphologies, which depend on the film preparation protocol, evolved. Finally, Ahn and Sancaktar[54] demonstrated with AFM that spin-coated PS-b-polyisoprene-b-PS triblock copolymer films reveal well-aligned three-dimensional nano-cylinders over the entire sample area.

For acrylate based, two component statistical copolymer films such knowledge does not exist, although acrylate based systems are frequently used as PSAs. At least, previous x-ray reflectivity (XRR) investigations of thicker films of this class of PSAs showed that the components are not homogeneously distributed along the film normal throughout the film.[55−57] For freshly solution cast samples, it is, with respect to the used solvent, the better soluble component which is enriched at the sample surface, whereas the component with the lower surface tension forms the top layer for aged samples. Unfortunately, information about lateral structures was not accessible with the employed methods. In contrast to that, in this study, the choice of the method GISAXS in combination with thin films, which allow for a full penetration of the x-rays, reveals a full morphological picture including the inner film structure. Similar to the study of Ahn and Sancaktar,[54] we find upright cylinders on the surface, too, but in our case, these are much more disordered in size and distance.

This article has the following structure: After a description of the investigated samples and a brief introduction in the experimental methods XRR, white light interferometry, GISAXS and mechanical tack test, the film morphology is described and quantified. Then, the resulting adhesive properties are presented and the corresponding thickness dependence is discussed. The article concludes with a summary of the results and a short outlook.

2. EXPERIMENTAL SECTION

2.1. Sample Preparation. The statistical copolymer P(nBA-stat-MA) with a molecular weight of M_w = 600 kg/mol is chosen as a PSA model system[58] for the thickness series presented in this study. In detail, the polymer chains are composed of 79.7% n-butyl acrylate (nBA), 20% methyl acrylate (MA) and 0.3% photoinitiator. The statistical copolymer was polymerized using a radical solution polymerization technique (semi-batch procedure in iso-butanol at 100 °C and 70% solids content with a peroxide starter) and thus shows a broad molecular weight distribution of 13.6, which is typical for adhesive applications.

Six different toluene based solutions of P(nBA-stat-MA) were prepared for spin-coating using concentrations of 12.5, 31.2, 55, 78.1, 110, and 220 g/L. The film thickness increases linearly with solution concentration,[59] so that each concentration corresponds to one film thickness of the sample series. For the XRR, GISAXS and probe tack experiments, the polymer films were spin-coated on microscope glass slides (76 mm × 26 mm × 1 mm, Menzel, Braunschweig, Germany) for 30 s at 2000 rpm under ambient conditions. For the white light interferometry measurements, the spin-coating was performed under the same conditions but on silicon with a silicon oxide layer, because for this method a higher reflectance of the substrate is required.

Shortly before the coating step, all substrates were cleaned using the following protocol: first, they remained 15 min in a bath consisting of 70 mL of H_2O_2 (30%), 165 mL of H_2SO_4 (96%), and 45 mL of deinoized water which was heated up to 80 °C. To remove possible residues of the bath, the substrates were carefully rinsed with deionized water and dried with compressed nitrogen.[60] Thus chemically the surfaces in contact with the polymer are similar.

In order to rule out aging[55] of the sample and thus, not comparable conditions, all samples were stored for approximately 10 days in a closed cabinet under constant temperature before the individual measurements.

2.2. X-ray Reflectivity (XRR). For the determination of the film thickness of the four thinnest films, x-ray reflectivity (XRR) measurements[61] were carried out on a Siemens D5000 Diffractometer. The x-ray wavelength was 0.154 nm which corresponds to the Cu−K_α

line. Beam collimation and shaping was realized with a slit system and a tantalum knife edge. For small incident angles, an absorber reducing the intensity by a factor of approximately 100 was used in order to avoid detector saturation and thus, wrong counting rates.

The reflectivity curves covered a range of incident angles of $0° < \varphi < 3°$ with a resolution of 0.005°. Because the counting rates for higher φ values were significantly lower, the angular range was divided into three overlapping regions with increased counting time for the higher angles. The corresponding data were finally merged according to the selected integration times.

2.3. White Light Interferometry (WLI). The film thickness of the two thickest films was measured with white light interferometry[62] (WLI). For this purpose an "F20 Thin-Film Measurement System" (Filmmetrics Inc., San Diego, USA) was mounted on top of a sample chamber (60 mm × 60 mm) equipped with a suitable hole to irradiate the sample. Like this, possible disturbances of the experiment originating from a slight wobbling of the interferometer were avoided. The spot size of the light beam could be varied between 0.5 and 10 mm and the maximal accessible wavelength range with the used setup was between 340 and 1100 nm.

2.4. Grazing Incidence Small Angle X-Ray Scattering (GISAXS). To analyze the morphology of the PSA ultrathin films grazing incidence small angle x-ray scattering (GISAXS) experiments[37−41,63−73] were carried out at the beamline BW4 at HASYLAB (DESY, Hamburg, Germany).[74,75] A monochromatic x-ray beam with a size of 40 μm × 20 μm and a wavelength of $\lambda = 0.138$ nm impinged under an incident angle $\alpha_i = 0.36°$ on the sample surface. The incident angle was chosen to be well above the critical angles of the components of the copolymer (α_c(PnBA) = 0.141° and α_c(PMA) = 0.149°) so that the beam fully penetrated the polymer film.[37] The diffusely scattered intensity was recorded on a two-dimensional (2D) MarCCD detector (2048 × 2048 pixels with a pixel size of 79 × 79 μm^2) which was positioned at a distance of 2003 mm measured from the probed spot of the sample. The detector was protected from the specularly reflected intensity by a point-like beamstop.

Each point on the detector was located using the coordinates (α_f, ψ). α_f is the exit angle which defines the z-direction (perpendicular to sample surface), and ψ is the out-of-plane angle pointing in y-direction, respectively (see Figure 2).[37] Two prominent line cuts were extracted for which the intensity of five pixels was integrated to improve statistics. The first cut, which is referred to as vertical cut, was taken along α_f and coincides with the symmetry axis at $\psi = 0$. The second cut is called horizontal cut and was taken along ψ at $\alpha_f = \alpha_c$(PnBA). Because of the symmetry of the 2D GISAXS patterns, only the right half ($\psi > 0$) of the horizontal cut was used. It is common to show the line cuts as a function of the corresponding component of the scattering vector q (see Figure 4). These components are $q_z = 2\pi[\sin(\alpha_f) + \sin(\alpha_i)]/\lambda$ for the vertical cut and $q_y = 2\pi[\cos(\alpha_f)\sin(\psi)]/\lambda$ for the horizontal cut.

In order to further improve the statistics of the horizontal cut, two measurements were performed for each sample. The integration time of the first one (shown in Figure 3) was set to 3 min and the point-like beamstop was used for detector protection. Due to the strong difference in signal amplitude between large and small values of the angle ψ, a second measurement with an integration time of 20 min was carried out for which an additional, rod-like beamstop shielding the region around $\psi = 0$ was mounted. The horizontal cuts of the two measurements were merged accordingly. Previous test experiments had proven that such exposure times do not cause any radiation damage to the polymer films.

2.5. Probe Tack Test. The probe tack tests[35,36,76] were performed under room temperature conditions using a custom-designed apparatus. It was equipped with a "FGP XF-3030" force sensor and a cylindrical probe with a diameter of 2 mm fabricated of stainless steel. The cylinder bottom contacting the surface of the adhesive film was highly polished to a roughness of approximately 2 nm which was determined by atomic force microscopy. Parallelism of the cylinder bottom with respect to the sample surface was realized using three precision screws at a radial distance of 70 mm in combination with an optical microscopy observation of the contact area with a high magnification CCD camera.

Sufficient statistical significance of the values of the maximum stress as well as the tack energy was achieved by repeating the tack experiment for each sample at least 8 times. After each measurement, the position on the sample was changed in order to provide a fresh spot with an untouched PSA surface for the next measurement. At the same time, the punch was carefully cleaned with a soft tissue soaked with toluene so that possible PSA residues or dust particles were removed.

The experimental parameters were kept constant for all samples presented in this article. In detail, the punch approached and contacted the PSA surface at a velocity of 0.1 mm/s. Immediately after reaching a contact pressure of 1.27 MPa, the movement stopped. The punch remained precisely 10 s in the corresponding position without performing any further movements, before it was retracted with a speed of again 0.1 mm/s. During retraction, the stress, which is the force divided by the punch area, was recorded as a function of distance from the point of zero stress.

3. RESULTS AND DISCUSSION

To provide a precise description of the tackiness as a function of the film thickness, it is necessary to perform an accurate measurement of the film thicknesses. Because the layer thicknesses h cover a range of almost three orders of magnitude, sufficient precision for all investigated samples cannot be achieved by only one technique: for the thinner films ($h \leq 363$ nm), XRR is the ideal technique whereas for the thicker films WLI is most suitable.

3.1. Film Thickness Determination. The XRR data are analyzed with the reflectivity simulation and analysis tool Parratt32.[77] Due to the fixed wavelength of 0.154 nm the wavelength of the intensity oscillations in the XRR data, which are also referred to as Kiessig fringes, originating from the interference of x-rays that are reflected at either the PSA surface-air or the substrate-PSA interface, decreases with increasing film thickness. For sufficiently large values of h (on the order of some hundred nanometers), they are even too small to be resolved within the accessible angular resolution.

Therefore for the thicker films WLI is chosen. As it can be seen from Figure 1b, the data show prominent features which enable a reliable thickness determination. The data are analyzed using the software provided by the device manufacturer using a similar algorithm compared to the XRR data.

As a result, the film thicknesses determined with XRR are from top to bottom 44.4, 133, 243, and 363 nm (see Figure 1a). Figure 1b shows the WLI data, which reveal from top to bottom film thicknesses of 607 and 1543 nm. AFM measurements confirm the thicknesses of 363 and 607 nm.

3.2. Morphological Characterization. The morphology of the PSA films of different film thickness is determined with GISAXS measurements.[37−41] The 2D GISAXS data do not show pronounced Bragg peaks or other features caused by a high degree of order. Moreover, no strong dependence on the film thickness is found (see Figure 3a−c). Obviously, the PSA films having thicknesses of (a) 44.4, (b) 133, and (c) 363 nm exhibit similar film morphology. To extract this film morphology from the 2D GISAXS data a modeling is necessary. It turned out that a completely mixed inner morphology cannot explain the GISAXS data. Instead a structure has formed. To describe this weak micro-phase separation structure, we use a model which contains a one-dimensional paracrystal[78] of PMA cylinders on top of a relatively rough but homogeneous layer of P(nBA-stat-MA) copolymer. The best fit to the GISAXS data is achieved when two types of cylinders are introduced. Both sets

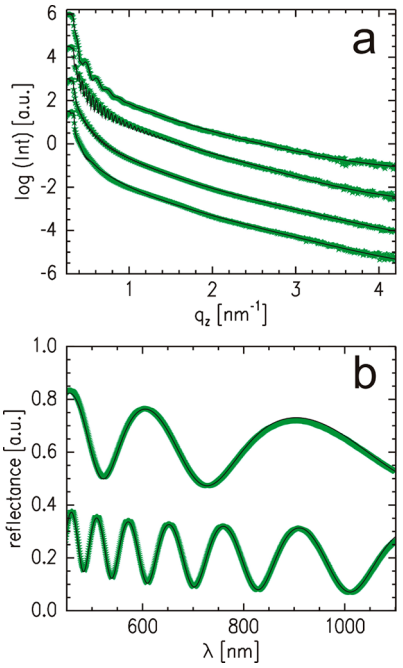

Figure 1. (a) XRR data (symbols) and corresponding fits (solid lines) for the determination of the layer thickness. For clarity, the data are shifted along the intensity axis. The thickness increases from top to bottom. (b) WLI data in analogy to panel a.

of objects do not contain identical monodisperse cylinders but exhibit a certain distribution of the radii R_1 and R_2, the center-to-center distance D as well as the height H. A schematic view of the PSA film morphology is illustrated in Figure 2.

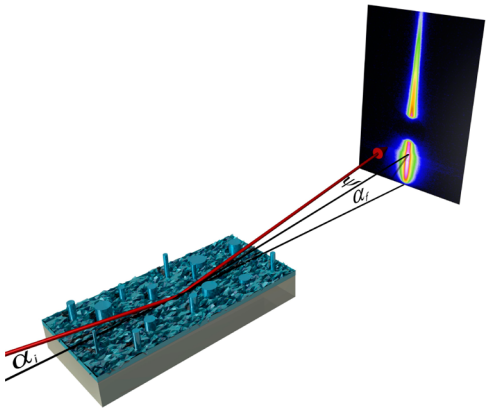

Figure 2. Schematic view of the GISAXS geometry shown together with one of the measured 2D GISAXS patterns. Furthermore, the sample morphology is illustrated. The relatively rough PSA film surface is decorated with cylindrical objects which are distributed in size and distance as explained in the main text.

In more detail, the diffusely scattered intensity in GISAXS geometry is calculated in the framework of the distorted wave Born approximation using the IsGISAXS software.[79,80] All structural lengths ξ (= H, R_1, R_2, or D), which in total provide a full description of the model, are assumed to follow a Gaussian distribution. For the calculation of the diffuse intensity distribution, 100 sampling points for each of the two radius distribution functions are taken into account. Furthermore, there are 50 points for the height distribution for each of the 200 sampling points of the radius. A fit to the data leads to a PSA film surface roughness of 5.6 nm for all investigated samples.

The measured 2D GISAXS data together with the corresponding simulations are depicted in Figure 3. The

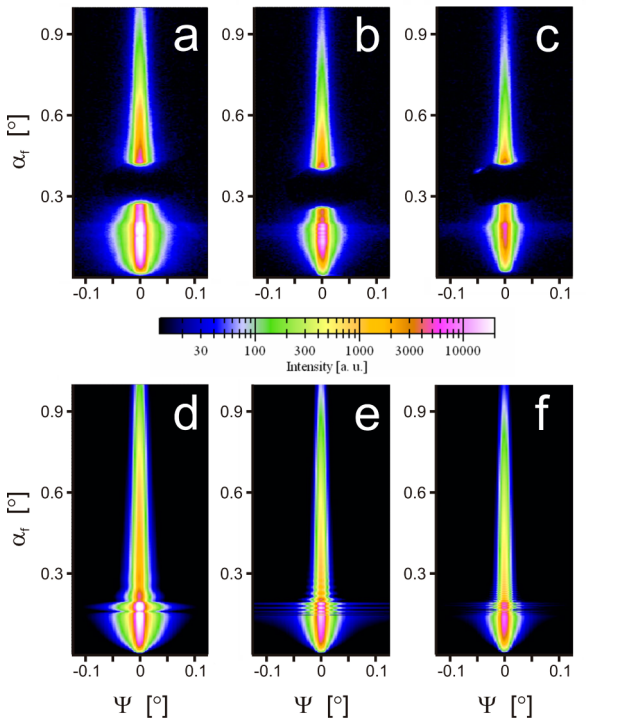

Figure 3. 2D GISAXS data from P(nBA-stat-MA) films with a thickness of (a) 44.4, (b) 133, and (c) 363 nm shown together with the best model fits (d–f). The intensity is shown on a logarithmic scale as indicated.

angular range as well as the color code for the intensity is the same for all six images. It has to be noted that specular reflection is not included in the IsGISAXS algorithm[79,80] and, thus, does not appear in the simulated images (see Figure 3d–f). In the measured data (Figure 3a–c), it is also not visible because it is blocked by a point-like beamstop as explained in the Experimental Section.

The good agreement between the 2D simulations and the measured GISAXS data is further illustrated by the vertical cut and the horizontal cut exemplarily shown for the sample with a thickness of 363 nm (see figure 4). As already mentioned, two types of cylinders are necessary to achieve such fit. The pronounced shoulder in the horizontal cut between $q_y = 10^{-2.4}$ and $10^{-1.4}$ nm^{-1} can only be fitted by including cylinders with a small and rather well-defined radius R_1 in the model. These small cylinders dominate the PSA film surface morphology. Cylinders of the second type are bigger and the radius R_2 is significantly broader distributed. These bigger cylinders are responsible for the shape of the overall intensity increase for small values of q_y. The overall probability of identifying a cylinder with radius R_1 is 99.5 %, while a probability of only 0.5 % for the large cylinders was found to successfully fit the GISAXS data. A fit of the refractive index of both types of cylinders clearly reveals that these cylindrical shaped objects consist of pure PMA.

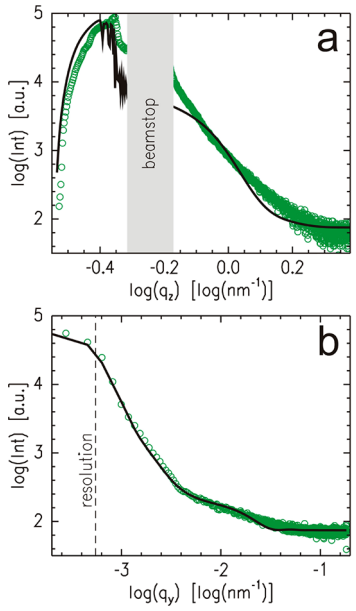

Figure 4. (a) Vertical cut of the measured (symbols) and simulated (solid line) 2D GISAXS data of the PSA film with a thickness of 363 nm. The grey area represents the region which is shielded by a point-like beamstop. (b) Corresponding horizontal cut of the measured (symbols) and simulated (solid line) 2D GISAXS data of the same sample. The dashed line indicates the resolution limit concerning large objects.

As already mentioned, the structural lengths ξ are very similarly distributed for all probed PSA film thicknesses. Figure 5 shows exemplarily the probability density distributions of R_1, R_2, and D for the sample with film thickness h = 363 nm. The differences in the full width half maximum as well as in the peak position are well visible. Also D is broadly distributed and as a consequence of only non-negative center-to-center distances, the mean center-to-center distance is slightly shifted as compared to the peak position.

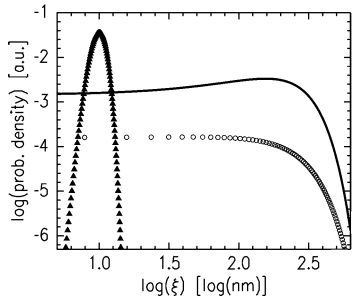

Figure 5. Probability distribution functions of the cylinder radii R_1 (filled triangles) and R_2 (open circles), as well as the center-to-center distance (solid line) of the cylinders corresponding to the IsGISAXS simulation for the sample with a thickness of 363 nm. Each symbol represents one sampling point for the simulation of the 2D GISAXS data.

For all investigated samples, the fitted parameters peak position and full width half maximum lead to a mean height covering the range 24 nm < H < 28 nm, and the mean radius R, which is calculated out of both distributions, R_1 and R_2, is 7 nm for the thinnest, and 11 nm for the thicker films. The difference arises entirely from the significantly smaller cylinders decorating the thinnest film. Finally, from the described distribution functions, the surface coverage κ is derived, which is a very good measure for the object density on the PSA surface. The corresponding range is 2.9% < κ < 3.3%.

Because in a statistical copolymer with some probability longer units of the monomer constituents exist, statistical copolymer films show a weak tendency to structure formation. For example in solution micelles can form and in films a surface induced enrichment was reported.[55−57] However, the formed micro-phase separation structure is strongly perturbed due to the fact that a statistical copolymer and not a well-defined block copolymer is under investigation. As a consequence, the formed cylinders have a broad size distribution and no regular lattice of cylinders is established as known from the micro-phase separation structures of diblock copolymers (with a small polydispersity). The absence of a lattice of cylinders explains why in the GISAXS no pronounced Bragg peaks occur (see Figure 3) and only a broad shoulder-like feature is seen (see Figure 4b).

Possibly, similar to our recent study about solution cast samples,[55−57] solubility effects lead to the fact that the PMA phase appears on top of the surface and prevent the formation of buried objects which purely consist of one of the two materials.

3.3. Tackiness as a Function of the Film Thickness.

These ultrathin PSA films do not only exhibit an interesting morphology but also the knowledge about their mechanical performance as adhesive films is an important issue for possible applications. For this purpose, probe tack tests are performed for six samples which only differ in thickness. Special care is taken for the alignment of the tack setup as described in the Experimental Section. The contact time in the tack experiment is limited to avoid reorganization of the copolymer in the bond state.

Figure 6a and b exemplarily show the measured stress as a function of the distance of the punch from the point of zero stress for all six PSA film thicknesses. All six probe tack curves are summarized in panel b of figure 6. Due to the large range of forces, which cover approximately two orders of magnitude, the data of the two thinnest films are only barely visible. These two curves are shown separately as a zoom-in in panel a. All stress-distance curves exhibit a peak-like shape. Possible modulations on the curves are within the error of the force and distance measurements.

Similar to tack curves probed for thick PSA films, the stress maximum is reached in the beginning of the retraction movement of the punch. Thus the general shape of a tack curve is still observed and as known from thick PSA films, the presence of a stress maximum will be related to cavitation.[25] However, in contrast to such classical tack experiments, there is no plateau region after the stress peak which would be attributed to the formation and elongation of fibrils.[25] The reason for the lack of the plateau is the drastically lower PSA volume that is available in ultrathin films, which prevents the formation of elongated structures. Thus the failure mechanism for such ultrathin PSA films is different to common PSA films. For the two thickest films (h = 607 and 1543 nm), the tack data does not differ within the achieved experimental accuracy, indicating that a bulk-like behavior could be reached.

The thickness dependence of the tackiness is quantified by extracting the parameters stress maximum F_{max}/A and tack energy W from the measured probe tack curves. The resulting values are shown on a logarithmic axis in Figure 6c and d. The data points represent the mean value of all measured curves

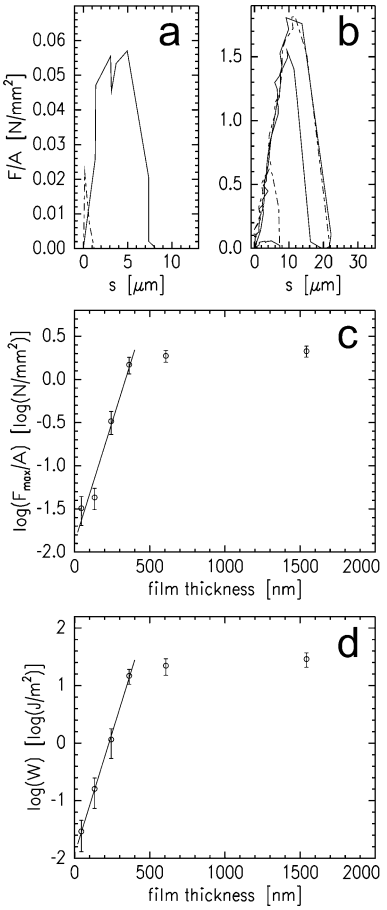

Figure 6. (a) Representative data of the probe tack tests for the film thickness h = 44.4 nm (dashed line) and h = 133 nm (solid line). (b) Representative tack data for each thickness in the sample series. The peak height increases with h. (c) Stress maximum as a function of film thickness. (d) Tack energy as a function of film thickness. The solid lines in panels c and d are linear fits through the first four data points indicating an exponential law behavior as explained in the main text.

corresponding to a certain film thickness and the error bar is calculated as the respective standard deviation. Both, the stress maximum and the tack energy remain constant for $h \geq 607$ nm. In contrast to that, below this threshold value, the performance of the PSA layer is very sensitive to the film thickness.

In more detail, the thickness dependence of both parameters $F_{max}(h)/A$ and $W(h)$ can be described with exponential laws: $F_{max}(h)/A = f_1 \exp\{f_2 h\}$ and $W(h) = w_1 \exp\{w_2 h\}$, respectively. The parameters f_1, f_2, w_1, and w_2 are derived from the linear fits in figures 6c and 6d. The resulting values are $f_1 = (1.31 \pm 0.46) \times 10^{-2}$ N/mm^2, $f_2 = (1.28 \pm 0.19) \times 10^{-2}$ nm^{-1}, $w_1 = (1.19 \pm 0.13) \times 10^{-2}$ J/m^2, and $w_2 = (1.94 \pm 0.04) \times 10^{-2}$ nm^{-1}. It has to be noted, however, that these power laws only hold within a certain thickness regime. As already explained, for $h > 363$ nm, both parameters saturate and it is obvious that the laws cannot be extrapolated for very small values of the film thickness h. The formulae would predict a non-zero tack energy for $h = 0$, so either there have to be some correction terms to the exponential law or there is also a lower limit for its validity.

To the knowledge of the authors, such type of thickness dependence with a critical thickness was not reported so far. One reason might be, that typically tack test experiments are restricted to thicker PSA films and films as thin as investigated in the present investigation are probed with very local techniques (e.g. so-called nano-tack or atomic force microscopic adhesion measurements). For copolymer based adhesives (thick films), the correlation of adhesive performance to large-strain mechanical response is much stronger than the correlation to linear viscoelastic properties.[27] Thus a direct comparison between local probes and tack is difficult.

4. CONCLUSION

Ultrathin films of a PSA model system consisting of a two-component statistical copolymer are processed via spin-coating. The influence of the film thickness, which is measured with XRR and WLI, on the morphology and the macroscopic tackiness is investigated.

GISAXS experiments prove that, in addition to the relatively high surface roughness of the PSA films, the surface is decorated with objects that are fully composed of the material representing the minority component of the copolymer. In other words, for the first time, weak phase separation in thin PSA statistical copolymer films is monitored. The fitting and simulation of the 2D GISAXS data give access to the exact distribution of the size and distance of these polymer objects. As a result, 3 % of the PSA surface is covered with objects (composed of MA) of approximately cylindrical shape and the dependence on the total PSA film thickness is only minor.

In contrast to that, the adhesive performance, which is monitored in probe tack tests, can be very sensitive with respect to the film thickness. All obtained stress-distance curves have a peak-like shape. The highest thickness sensitivity is observed for film thicknesses below 500 nm. In this regime, prominent parameters such as the stress peak or the tack energy follow an exponential law behavior. For thicker films, however, the tackiness remains constant within the probed thickness range.

One approach to link the structural information with the mechanical behavior might be based on the block model as introduced by Yamaguchi et al.[81] for the debonding process of the probe-tack test of a viscoelastic film. Instead of dividing the initial adhesive layer into N rectangular blocks of equal size,[81] the microstructure deduced from the structural analysis could be taken directly. With such an approach the investigation can be extended to other compositions of the copolymer, as all applied experimental techniques will work for different compositions of the PSA as well.

In summary, this investigation gives first important insights on the mechanical behavior of ultrathin acrylate-based adhesive layers. With respect to applications, it would be beneficial to find routes to optimize the performance of such ultrathin PSA films. It is likely that the film morphology can play a key role to achieve this goal.

AUTHOR INFORMATION

Corresponding Author

*Phone: +498928912451. Fax: +498928912473. E-mail: muellerb@ph.tum.de.

Notes

The authors declare no competing financial interest.

ACKNOWLEDGMENTS

We thank B. Russ and P. Böni for their assistance in the XRR measurements and BASF SE for donating the polymer sample. We thank Y. Peykova and N. Willenbacher for fruitful discussions. The financial support by the "Deutsche Forschungsgemeinschaft (DFG)" in the project MU1487/6 is

gratefully acknowledged. V.K. acknowledges financial support by BMBF project 05KS7W01.

REFERENCES

(1) Chaundry, M. K.; Whitesides, G. M. *Science* **1992**, *255*, 1230.
(2) Ferguson, G. S.; Chaundry, M. K.; Sigal, G. B; Whitesides, G. M. *Science* **1991**, *253*, 776.
(3) Newby, B. Z.; Chaundry, M. K.; Brown, H. R. *Science* **1995**, *269*, 1407.
(4) Shi, J.; Chan-Park, M. B.; Li, C. M. *ACS Appl. Mater. Interfaces* **2011**, *3*, 1880.
(5) Kentsch, J.; Dürr, M.; Schnelle, T.; Gradl, G.; Müller, T; Jäger, M.; Normann, A; Stelze, M. *IEE Proc.:Nanobiotechnol.* **2003**, *150*, 82.
(6) Dreuth, H.; Heiden, C. *Mater. Sci. Eng. C* **1998**, *5*, 227.
(7) Uddin, M. A.; Ho, W. F.; Chan, H. P. *J. Mater. Sci.: Mater. Electron.* **2007**, *18*, 655.
(8) Johnson, P. M.; Stafford, C. M. *ACS Appl. Mater. Interfaces* **2010**, *2*, 2108.
(9) Chan, E. P.; Kundu, S.; Lin, Q.; Stafford, C. M. *ACS Appl. Mater. Interfaces* **2011**, *3*, 331.
(10) Binder, K.; Horbach, J.; Vink, R; De Virgiliis, A. *Soft Matter* **2008**, *4*, 1555.
(11) Wu, W.; van Zanten, J. H.; Orts, W. J. *Macromolecules* **1995**, *28*, 771.
(12) Kim, J. H.; Jang, J.; Zin, W.-C. *Langmuir* **2000**, *16*, 4604.
(13) Kawana, S.; Jones, R. A. L. *Phys. Rev. E* **2001**, *63*, 021501.
(14) Forrest, J. A.; Dalnoki-Veress, K.; Dutcher, J. R. *Phys. Rev. E* **1997**, *56*, 5705.
(15) Forrest, J. A.; Dalnoki-Veress, K.; Dutcher, J. R. *Phys. Rev. E* **1998**, *58*, 6109.
(16) Tress, M.; Erber, M.; Mapesa, E. U.; Huth, H.; Müller, J.; Serghei, A.; Schick, C.; Eichhorn, K.-J.; Voit, B.; Kremer, F. *Macromolecules* **2010**, *43*, 9937.
(17) Mapesa, E. U.; Erber, M.; Tress, M.; Eichhorn, K.-J.; Serghei, A.; Voit, B.; Kremer, F. *Eur. Phys. J. Special Topics* **2010**, *189*, 173.
(18) Akabori, K.; Tanaka, K.; Kajiyama, T.; Takahara, A. *Macromolecules* **2003**, *36*, 4937.
(19) Yamada, S.; Nakamura, G; Amiya, T. *Langmuir* **2001**, *17*, 1693.
(20) Luengo, G.; Schmitt, F.-J.; Hill, R.; Israelachvili, J. *Macromolecules* **1997**, *30*, 2482.
(21) Domke, J; Rademacher, M. *Langmuir* **1998**, *14*, 3320.
(22) Stafford, C. M.; Vogt, B. D.; Harrison, C.; Julthongpiput, D.; Huang, R. *Macromolecules* **2006**, *39*, 5095.
(23) Chan, E. P.; Page, K. A.; Im, S. H.; Patton, D. L.; Huang, R.; Stafford, C. M. *Soft Matter* **2009**, *5*, 4683.
(24) Bodiguel, H.; Fretigny, C. *Macromolecules* **2007**, *40*, 7291.
(25) Creton, C. *MRS Bull.* **2003**, *28*, 434.
(26) Shull, K.R.; Creton, C. *J. Polym. Sci. B* **2004**, *42*, 4023.
(27) Creton, C.; Hu, G. J.; Deplace, F.; Morgret, L.; Shull, K.R. *Macromolecules* **2009**, *42*, 7615.
(28) Peykova, Y.; Lebedeva, O.V.; Diethert, A.; Müller-Buschbaum, P.; Willenbacher, N. *Int. J. Adhes. Adhes.* **2012**, *34*, 116.
(29) Bates, F. S.; Fredrickson, G. H. *Ann. Rev. Phys. Chem.* **1990**, *41*, 557.
(30) Phillips, J. P.; Deng, X.; Stephen, R. R.; Fortenberry, E. L.; Todd, M. L.; McClusky, D. M.; Stevenson, S.; Misra, R.; Morgan, S.; Long, T. E. *Polymer* **2007**, *48*, 6773.
(31) Wang, X. P.; Xiao, X.; Tsui, O. K. C. *Macromolecules* **2001**, *34*, 4180.
(32) Portigliatti, M.; Koutsos, V.; Hervet, H.; Léger, L. *Langmuir* **2000**, *16*, 6374.
(33) Chung, J. Y.; Kim, K. H.; Chaundry, M. K.; Sarkar, J.; Sharma, A. *Eur. Phys. J. E* **2006**, *20*, 47.
(34) Crosby, A. J; Shull, K. R. *J. Polym. Sci., Polym. Phys.* **1999**, *37*, 3455.
(35) Webber, R. E.; Shull, K. R; Roos, A.; Creton, C. *Phys. Rev. E* **2003**, *68*, 021805.
(36) Crosby, A. J.; Shull, K. R.; Lakrout, H.; Creton, C. *J. Appl. Phys.* **2000**, *88*, 2956.
(37) Müller-Buschbaum, P. *Anal. Bioanal. Chem.* **2003**, *376*, 3.
(38) Müller-Buschbaum, P.; Gutmann, J.S.; Cubitt, R.; Stamm, M. *Colloid. Polym. Sci.* **1999**, *277*, 1193.
(39) Park, S.; Kim, K.; Kim, D. M.; Kwon, W.; Choi, J.; Ree, M. *ACS Appl. Mater. Interfaces* **2011**, *3*, 765.
(40) Fischereder, A.; Rath, T.; Haas, W.; Amenitsch, H.; Schenk, D.; Zankel, A.; Saf, R.; Hofer, F.; Trimmel, G. *ACS Appl. Mater. Interfaces* **2012**, *4*, 382.
(41) Patel, R. N.; Heitsch, A. T.; Hyun, C.; Smilgies, D.-M.; Lozanne, A.; de; Loo, Y.-L.; Korgel, B. A. *ACS Appl. Mater. Interfaces* **2009**, *1*, 1339.
(42) Phillip, W. A.; O'Neill, B.; Rodwogin, M.; Hillmyer, M. A.; Cussler, E. L. *ACS Appl. Mater. Interfaces* **2010**, *2*, 847.
(43) Metwalli, E.; Perlich, J.; Wang, W.; Diethert, A.; Papadakis, C. M.; Müller-Buschbaum, P. *Macromol. Chem. Phys.* **2010**, *211*, 2102.
(44) Lin, Y.; Böker, A.; He, J.; Sill, K.; Xiang, H.; Abetz, C.; Li, X.; Wang, J.; Emrick, T.; Long, S.; Wang, Q.; Balazs, A.; Russell, T. P. *Nature* **2005**, *434*, 55.
(45) Kelly, J. Y.; Albert, J. N. L.; Howarter, J. A.; Kang, S.; Stafford, C. M.; Epps, T. H., III; Fasolka, M. J. *ACS Appl. Mater. Interfaces* **2010**, *2*, 3241.
(46) Lee, M.; Park, J. K.; Lee, H.-S.; Lane, O.; Moore, R. B.; McGrath, J. E.; Baird, D. G. *Polymer* **2009**, *50*, 6129.
(47) Isono, Y.; Tanisugi, H.; Endo, K.; Fujimoto, T.; Hasegawa, H.; Hashimoto, T.; Kawai, H. *Macromolecules* **1983**, *16*, 5.
(48) Müller-Buschbaum, P.; Gutmann, J. S.; Stamm, M. *Macromolecules* **2000**, *33*, 4886.
(49) Ade, H.; Zhang, X.; Cameron, S.; Costello, C.; Kirz, J.; Williams, S. *Science* **1992**, *258*, 972.
(50) Kraus, G.; Jones, F. B.; Marrs, O. L.; Rollmann, K. W. *J. Adhes.* **1977**, *8*, 235.
(51) Müller-Buschbaum, P.; Bauer, E.; Pfister, S.; Roth, S. V.; Burghammer, M.; Riekel, C.; David, C.; Thiele, U. *Europhys. Lett.* **2006**, *73*, 35.
(52) Müller-Buschbaum, P.; Bauer, E.; Maurer, E.; Roth, S. V.; Gehrke, R.; Burghammer, M.; Riekel, C. *J. Appl. Cryst.* **2007**, *40*, s341.
(53) Escalé, P.; Save, M.; Lapp, A.; Rubatat, L. *Soft Matter* **2010**, *6*, 3202.
(54) Ahn, D. U.; Sancaktar, E. *Soft Matter* **2008**, *4*, 1454.
(55) Diethert, A.; Peykova, Y.; Willenbacher, N.; Müller-Buschbaum, P. *ACS Appl. Mater. Interfaces* **2010**, *2*, 2060.
(56) Diethert, A.; Ecker, K.; Peykova, Y.; Willenbacher, N.; Müller-Buschbaum, P. *ACS Appl. Mater. Interfaces* **2011**, *3*, 2012.
(57) Diethert, A.; Müller-Buschbaum, P. *J. Adhes.* **2011**, *87*, 1067.
(58) Peykova, Y.; Guriyanova, S.; Lebedeva, O. V.; Diethert, A.; Müller-Buschbaum, P.; Willenbacher, N. *Int. J. Adhes. Adhes.* **2010**, *30*, 245.
(59) Ruderer, M. A.; Hirzinger, M.; Müller-Buschbaum, P. *Chem. Phys. Chem.* **2009**, *10*, 2692.
(60) Müller-Buschbaum, P. *Eur. Phys. J. E* **2003**, *12*, 443.
(61) Parratt, L. G. *Phys. Rev.* **1954**, *95*, 359.
(62) van den Berg, A. M. J.; Smith, P. J.; Perelaer, J.; Schrof, W.; Koltzenburg, S.; Schubert, U. S. *Soft Matter* **2007**, *3*, 238.
(63) Roth, S. V.; Müller-Buschbaum, P.; Burghammer, M.; Walter, H.; Panagiotou, P.; Diethert, A.; Riekel, C. *Spectrochim. Acta B* **2004**, *59*, 1765.
(64) Müller-Buschbaum, P.; Roth, S. V.; Burghammer, M.; Diethert, A.; Panagiotou, P.; Riekel, C. *Europhys. Lett.* **2003**, *61*, 639.
(65) Olsen, B. D.; Li, X.; Wang, J.; Segalman, R. A. *Soft Matter* **2009**, *5*, 182.
(66) Lee, B.; Park, I.; Yoon, J.; Park, S.; Kim, J.; Kim, K.-W.; Chang, T.; Ree, M. *Macromolecules* **2005**, *38*, 4311.
(67) Ahn, H.; Shin, C.; Lee, B.; Ryu, D. Y. *Macromolecules* **2010**, *43*, 1958.
(68) Stein, G. E.; Lee, W. B.; Fredrickson, G. H.; Kramer, E. J.; Li, X.; Wang, J. *Macromolecules* **2007**, *40*, 5791.
(69) Renaud, G.; Lazzari, R.; Revenant, C.; Barbier, A.; Noblet, M.; Ulrich, O.; Leroy, F.; Jupille, J.; Borensztein, Y.; Henry, C. R.; Deville,

J.-P.; Scheurer, F.; Mane-Mane, J.; Furchart, O. *Science* **2003**, *300*, 1416.
(70) Renaud, G.; Lazzari, R.; Leroy, F. *Surf. Sci. Rep.* **2009**, *64*, 255.
(71) Okuda, H.; Kato, M.; Kuno, K.; Ochiai, S.; Usami, N.; Nakajima, K.; Sakata, O. *J. Phys.: Condens. Matter* **2010**, *22*, 474003.
(72) Weber, C. H. M.; Liu, F.; Zeng, X. B.; Ungar, G.; Mullin, N.; Hobbs, J. K.; Jahr, M.; Lehmann, M. *Soft Matter* **2010**, *6*, 5390.
(73) Yager, K. G.; Fredin, N. J.; Zhang, X. H.; Berry, B. C.; Karim, A.; Jones, R. L. *Soft Matter* **2010**, *6*, 92.
(74) Perlich, J.; Rubeck, J.; Botta, S.; Gehrke, R.; Roth, S. V.; Ruderer, M. A.; Prams, S. M.; Rawolle, M.; Zhong, Q.; Körstgens, V.; Müller-Buschbaum, P. *Rev. Sci. Instrum.* **2010**, *81*, 105105.
(75) Roth, S. V.; Döhrmann, R.; Dommach, M.; Kuhlmann, M.; Kröger, I.; Gehrke, R.; Walter, H.; Schroer, C.; Lengeler, B.; Müller-Buschbaum, P. *Rev. Sci. Instrum.* **2006**, *77*, 085106.
(76) Maurer, E.; Loi, S.; Wulff, D.; Willenbacher, N.; Müller-Buschbaum, P. *Phys. B* **2005**, *357*, 144.
(77) Braun, C. *Parratt32*, version 1.6: HMI: Berlin, 2002.
(78) Hosemann, R.; Vogel, W.; Weick, D.; Baltá-Calleja, F. J. *Acta Crystallogr.* **1981**, *A37*, 85.
(79) Lazzari, R. *J. Appl. Cryst.* **2002**, *35*, 406.
(80) Kaune, G.; Ruderer, M. A.; Metwalli, E.; Wang, W.; Couet, S.; Schlage, K.; Röhlsberger, R.; Roth, S. V.; Müller-Buschbaum, P. *ACS Appl. Mater. Interfaces* **2009**, *1*, 353.
(81) Yamaguchi1, T.; Morita1, H.; Doi, M. *Eur. Phys. J. E* **2006**, *20*, 7.